Supporting Information

***In Situ* Growth of Cobalt Phosphide (CoP) on Perovskite Nanofibers as An Optimized Trifunctional Electrocatalyst for Zn-Air Batteries and Overall Water Splitting**

Catalyst ink preparation. To prepare the catalyst ink, 10 mg of the as-synthesized perovskite was mixed with 10 mg of carbon black (Cabot). The mixture was dispersed in a solution containing 200 µL of 5wt. % Nafion (Aldrich) and 800 µL of isopropyl alcohol (Fisher Scientific Cooperation), and then sonicated for an hour. The glassy carbon rotating disk electrode (5 mm RDE, Pine instrument) was pre-polished with 0.3 and 0.05 µm aluminum oxide suspension and rinsed with deionized water to obtain a mirror-like surface. 5 µL of the catalysts ink was dispersed on a 5 mm pre-polished glassy carbon rotating disk electrode (RDE, Pine instrument) and was dried in air for 1 h before the test. The loading amount of the perovskite catalyst was 0.255 mg_{ox} cm^{-2}.

Electrochemical measurements. The HER, ORR and OER measurements were performed using an impedance/gain-phase analyzer (Solartron 1255) and an electrochemical interface (Solartron 1287). The electrochemical tests were carried with a standard three-electrode cell, where the catalyst-coated glassy carbon RDE, the Ag/AgCl (Sat. KCl) electrode and Pt wire served as the working electrode, the reference electrode and the counter electrode, respectively. The HER and OER were conducted using both 0.1 M KOH and 1 M KOH electrolyte, while the ORR was measured using a 0.1 M KOH electrolyte. For the ORR and OER tests, the oxygen saturated 0.1 M KOH solution was prepared via purging pure oxygen (99.9 %) into the electrolyte for 30 min.

Linear sweep voltammetry (LSV) was conducted in a voltage scan range of 0.1 V to -0.8 V (vs. Ag/AgCl, sat. KCl) with rotating speeds of 400, 900, 1600 and 2500 rpm. For OER measurements, LSVs were measured in a voltage range of 0.1 to 1 V vs. Ag/AgCl at a scan rate of 20 mV s^{-1}. While for HER measurements, the LSVs were measured from -0.8 to -1.6 V vs. Ag/AgCl at a scan rate of 20 mV s^{-1} in Ar-saturated KOH solution.

Rechargeable zinc-air battery assembly and tests. A homemade rechargeable zinc-air battery was constructed, with a zinc plate anode and an electrocatalyst coated GDL cathode. The cell was filled with 6 M KOH and 0.2 M zinc acetate to ensure reversible Zn electrochemical reaction. The catalyst inks for the rechargeable zinc air battery (2 mg mL^{-1}) were prepared by sonicating 10 mg electrocatalysts, 3 mL isopropyl alcohol, 1 mL deionized water and 1 mL of 5.0 wt% Nafion (Aldrich). The cathode was prepared by drop casting the catalyst inks onto the center area of GDL (7/16" in diameter), followed by drying under ambient condition until a mass loading of 0.5 mg cm^{-2} was achieved. The battery tests were conducted by sweeping LSVs at 10 mV s^{-1} with Solartron 1287. The galvanostatic discharge-charge cycling was measured at a current density of 10mA cm^{-2}, and each cycle was set to be 10 min charge and 10 min discharge.

Water splitting tests. The full water splitting test was conducted in 1 M KOH solution, the electrocatalysts was loaded on Ni foam electrodes with a mass loading of 2 mg cm^{-2}. The on CoP-PBSCF loaded Ni foam was applied as both anode and cathode in the full water splitting test. For comparison, the RuO_2/C and Pt/C loaded Ni foam was applied as anode and cathode, respective.

Characterization. The X-ray diffraction (XRD) measurements were performed on a Rigaku Rotaflex X-ray diffractormeter using Cu Kα radiation at 40 kV and 44 mA. The morphology and structure of the samples were characterized using a Zeiss Sigma 300 VP Field Emission SEM

(FESEM) and a JEOL JEM-ARM200CF Atomic Resolution S/TEM. X-ray photoelectron spectroscopy (XPS) measurements were performed using Kratos AXIS to examine the surface chemistry of the sample. The XPS spectra were referenced to the C 1s bonding energy (284.8 eV). The BET specific surface areas and pore size were evaluated using an Autosorb Quantachrome 1MP apparatus.

DFT calculations. The first-principle calculations were carried out with the Vienna *ab initio* Simulation Package (VASP).[1–4] The electron wavefunctions were presented by the planewave basis set with an energy cutoff of 520 eV. The ionic cores and their interaction with the valence electrons were treated with the projector-augmented plane-wave (PAW) method.[5,6] The Perdew-Burke-Ernzerhof (PBE) generalized gradient approximation functional (GGA) was employed to describe the exchange–correlation interactions.[7] The spin polarization was enabled in all the calculations. The Monkhorst-Pack K-point mesh of $3\times5\times3$ was used for the $PBSCFO_6$ unit cell.[8–10] The occupancy of the one-electron states was calculated using an electronic temperature of k_BT = 0.05 eV, while all the energies were extrapolated to T = 0 K. The structures were geometrically optimized until the force components were less than 0.06 eV/Å. The relaxed lattice constants of the $PBSCFO_6$ unit cell are a=7.664 Å, b=3.850 Å and c=7.663 Å, in good agreement with the experimental results obtained in this study, further confirming the reasonability of the above computational setups. Based on the fully relaxed unit cell, the (001) slab model was built with the vacuum thickness of 15 Å along the z axis to minimize the periodic image interactions. The slab contains seven atomic layers with Co/Fe-O as the surface termination layer. During the geometry optimization of the slab models, the bottom three atomic layers were constraint, whereas the above four layers were allowed to relax.

The effective p band center of the oxygen within the first atomic layer of the surface models was determined by taking the centroid of the projected density of states of the oxygen p states relative to the Fermi level using the commonly used formula,[10–13]

$$band\ center = \frac{\int E \cdot f(E) dE}{\int f(E) dE}$$

Where E and $f(E)$ are the electron energy and the corresponding PDOS value, respectively.

For the purpose of this study, the CoP and CoOH adsorbed surface models were subsequently built and relaxed to simulate the exsolutions of CoP on the surface of $PBSCFO_6$,[14,15] where the O p band center was calculated for the surrounding oxygen in the first layer. Moreover, to compare the catalytic activities of the three typical surfaces for hydrogen evolution reaction (HER), the Gibbs free energy diagram for HER was constructed which has been verified capable of reflecting the relative activity trend of the catalysts.[16,17] Both the Co and Fe sites on the surface were taken as the catalytic active centers for HER with the adsorption of the intermediate H at a surface coverage of 0.25.[10] The ΔG_{H*} was then calculated as,[16,18]

$$\Delta G_{H*} = E_{H*} - E* - \frac{E_{H_2}}{2} + \Delta(E_{ZPE} + \int C_p dT - TS)$$

where E_{H*}, $E*$ and E_{H_2} are the DFT calculated electronic energies of the H adsorbed surface, the bare surface and hydrogen gas, respectively; E_{ZPE} is the zero-point vibrational energy; $\int C_p dT$ is the enthalpy correction; TS is the entropy contribution. The relevant entropy and enthalpy corrections were calculated with the suggested methods by the previous studies.[19,20]
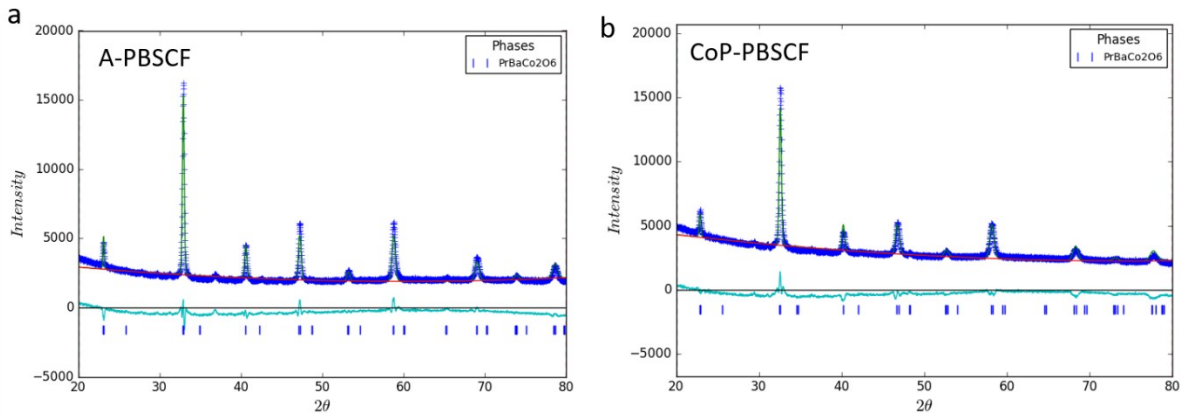
Figure S1. XRD refinement data of (a) A-PBSCF and (b) CoP-PBSCF.
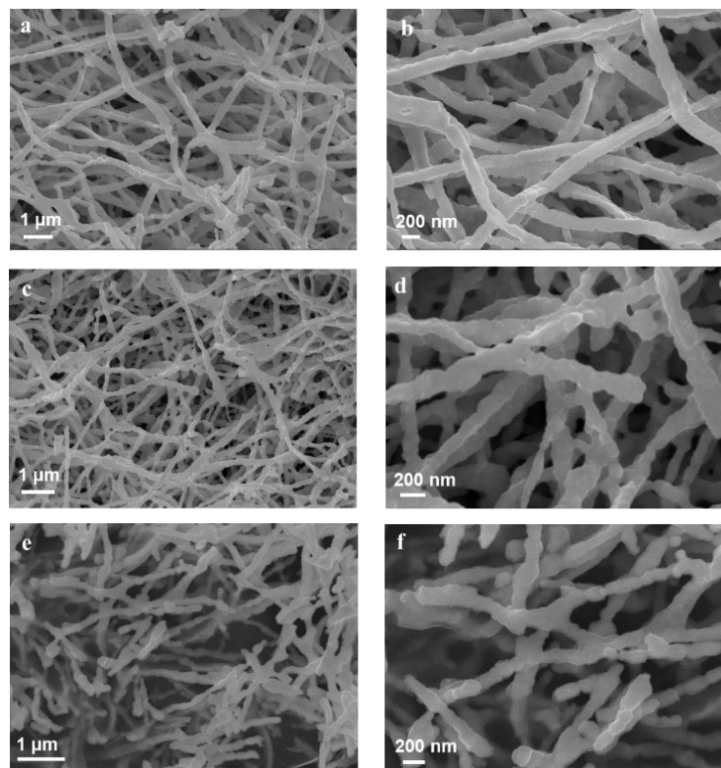
Figure S2. (a) and (b) FESEM image of A-PBSCF; (c) and (d) FESEM image of H-PBSCF; (e) and (f) FESEM image of CoP- PBSCF.
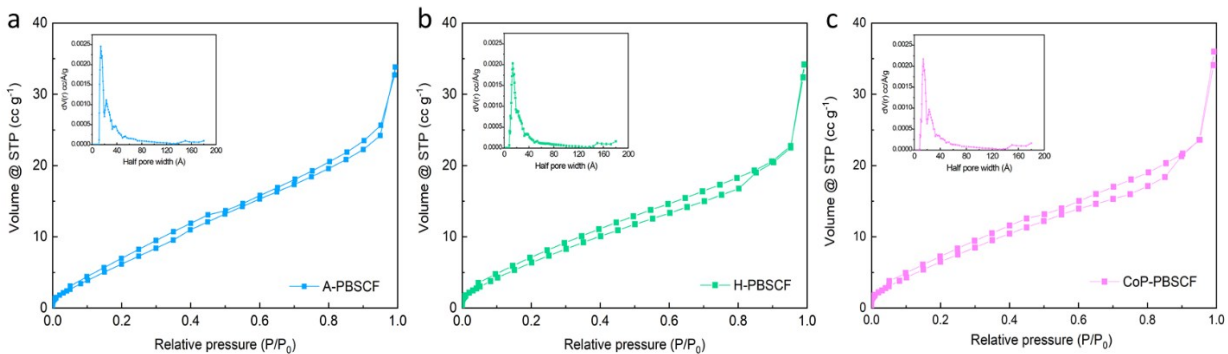
Figure S3. N_2 adsorption and desorption isotherm curves with BJH pore size distribution (inset) of (a) A-PBSCF, (b) H-PBSCF and CoP-PBSCF. The Brunauer−Emmett−Teller (BET) analysis reveals a specific surface area of 15.87 m^2 g^{-1} for CoP-PBSCF, similar to that of the A-PBSCF (16.20 m^2 g^{-1}) and H-PBSCF (15.43 m^2 g^{-1}).
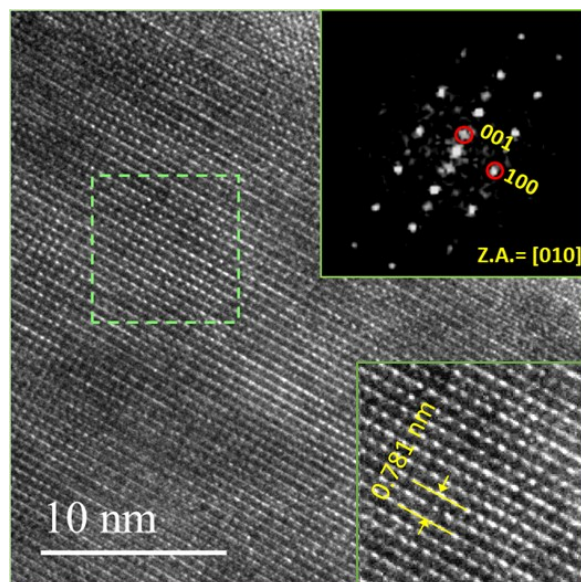
Figure S4. HRTEM images of the A-PBSCF and the corresponding diffractogram.
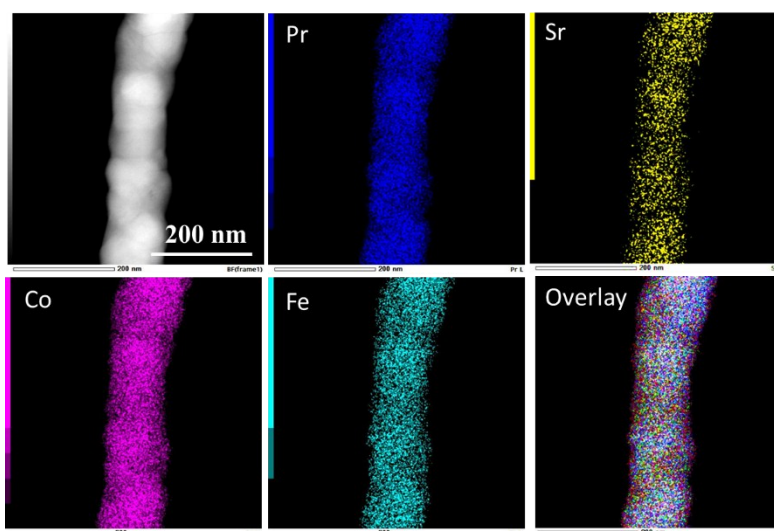
Figure S5. High-angle annular dark field-scanning transmission electron microscope (HAADF-STEM) image and the corresponding EDX elemental mapping profiles of A-PBSCF nanofiber calcined at 900 °C.
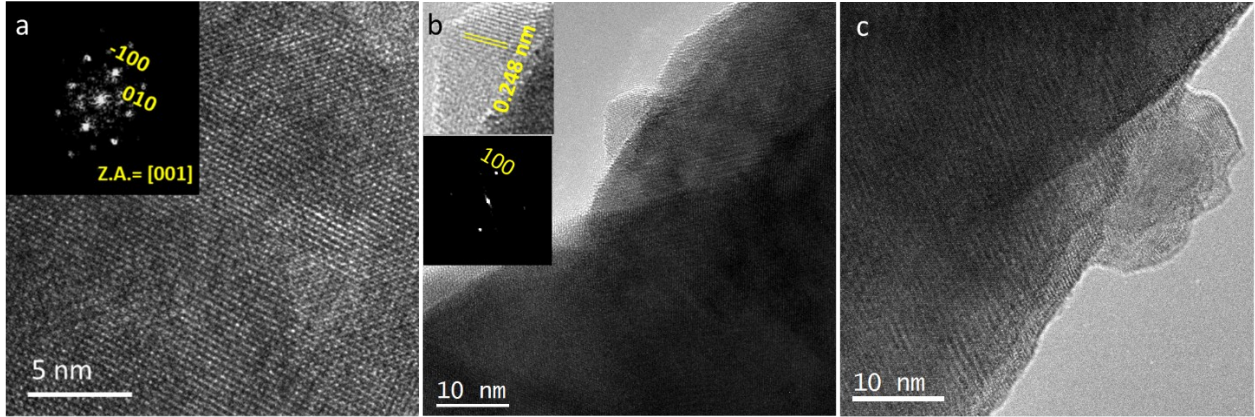
Figure S6. HRTEM images of H-PBSCF and the corresponding diffractogram. The exsolved NP shows a spacing of d=0.248 nm corresponding to (100) of Co (see the index in the FFT and the inserted HRTEM image in Figure S6b).
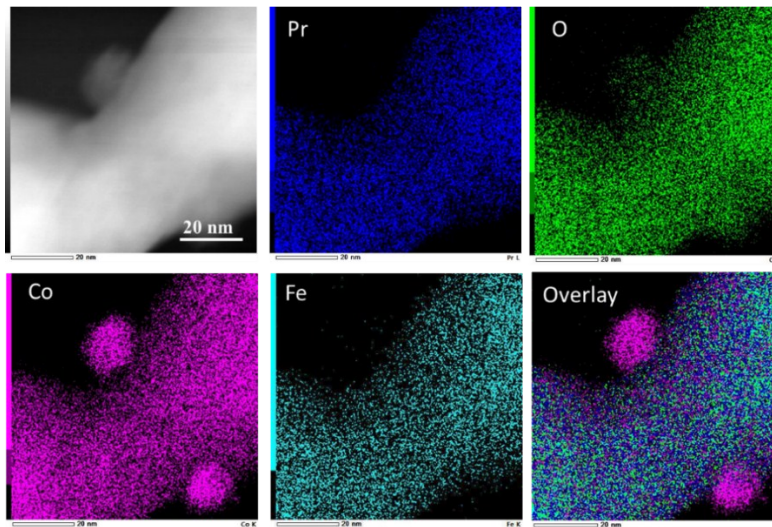
Figure S7. HAADF-STEM and EDX mapping of H-PBSCF.
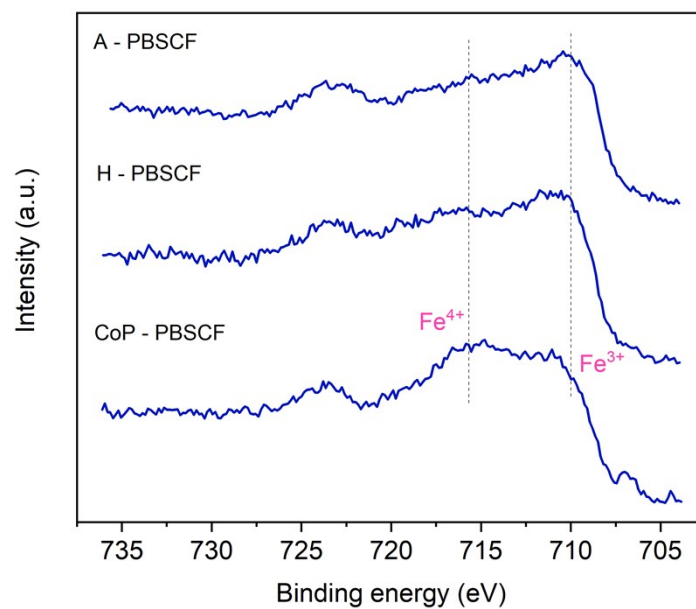
Figure S8. Fe 2p spectra of oxygen in A-PBSCF, H-PBSCF and CoP-PBSCF.
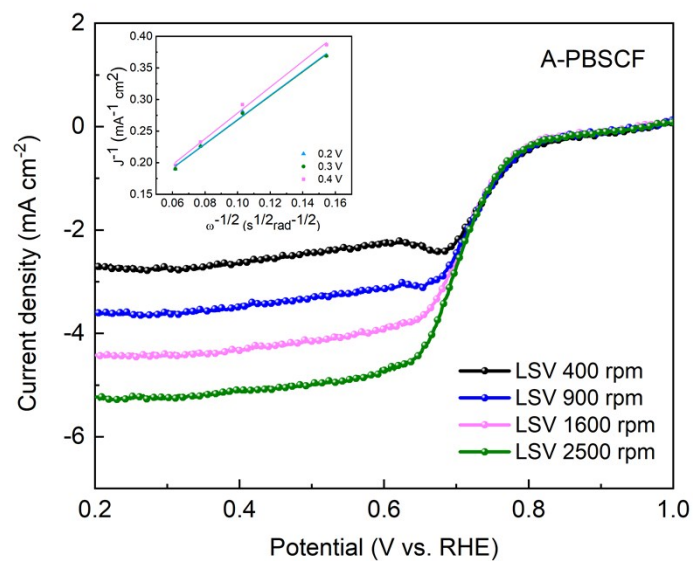
Figure S9. ORR LSV curves of PBSCF electrocatalysts at different rotation speed. Inset: K-L plots at various potentials.
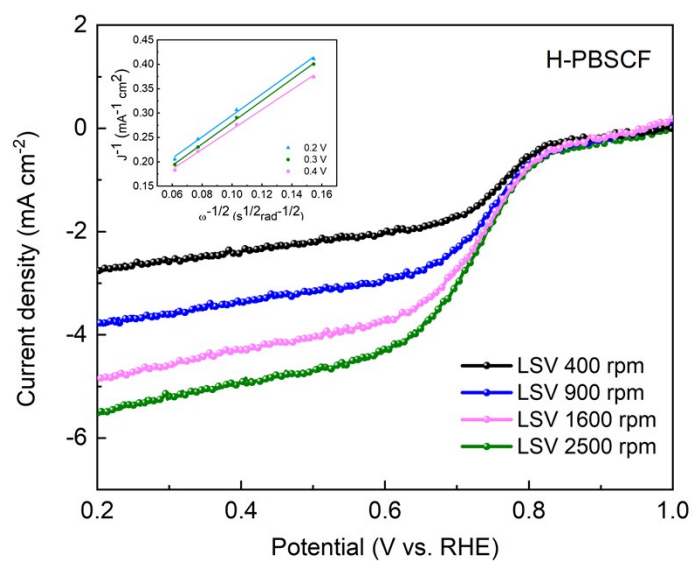
Figure S10. ORR LSV curves of H-PBSCF electrocatalysts at different rotation speed. Inset: K-L plots at various potentials.
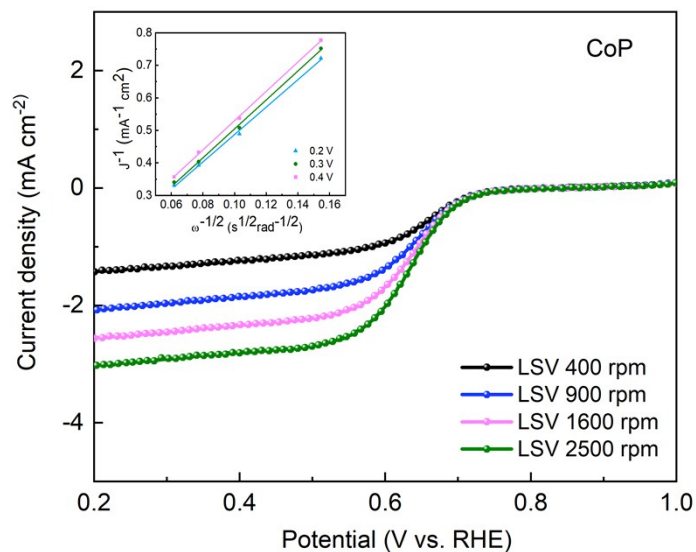
Figure S11. ORR LSV curves of CoP electrocatalysts at different rotation speed. Inset: K-L plots at various potentials.
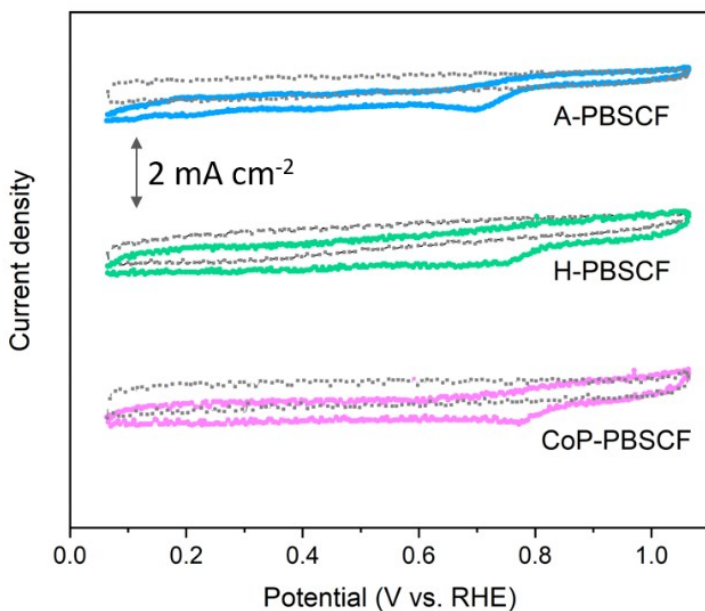
Figure S12. CV curves of PBSCF, H-PBSCF, CoP-PBSCF in O_2- and N_2-saturated 0.1 M KOH electrolyte for ORR.
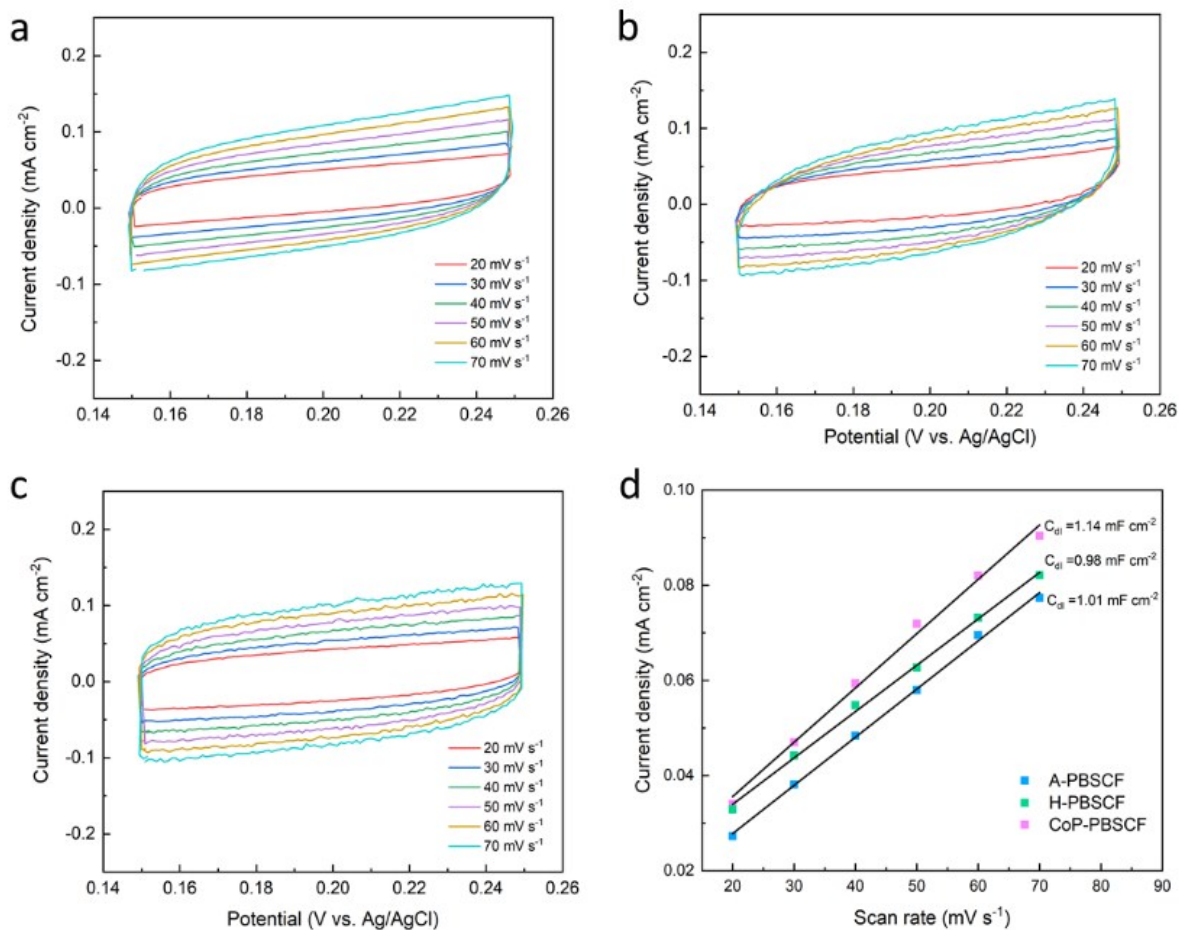
Figure S13. Electrochemical CV scans of (a) A-PBSCF, (b) H-PBSCF, and (c) CoP-PBSCF at a non-faradic potential range at different scan rates; (d) measurements of the electrochemical double-layer capacitance of samples at the potential of 0.20 V vs. Ag/AgCl at different scan rates. The current density refers to current density difference ($\Delta J/2 = (Ja-Jc)/2$) in figure d.
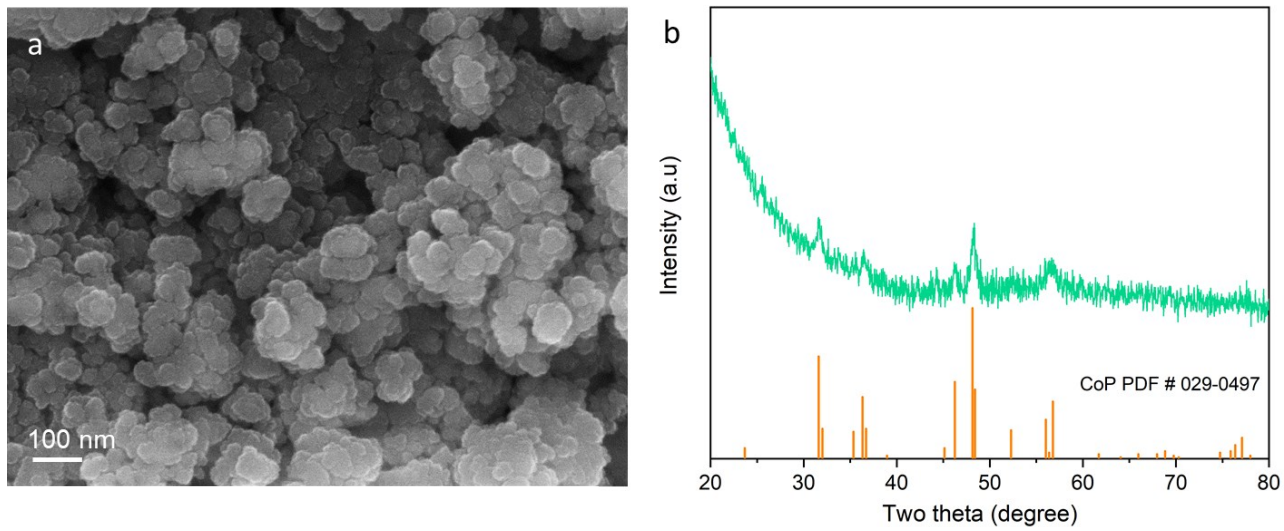
Figure S14. (a) FESEM image of the CoP NPs; (b) XRD pattern of the CoP NPs.

Table S1. The XRD Rietveld refinement results for A-PBSCF and CoP-PBSCF.

	Space group	a (Å)	b (Å)	c (Å)	V (Å)^3
A-PBSCF	*P4/mmm*	3.845	3.845	7.715	114.06
CoP-PBSCF	*P4/mmm*	3.891	3.891	7.739	117.17

Table S2. Summary of the overpotential (η) for OER @ 10 mA cm^{-2} on the catalysts in this work and other oxides in the literature.

Materials	Journal, Year, volume, first page	η	Electrolyte
Co_3O_4/N-rmGO	Nat. Mater., 2011, 10, 780	0.31 V	0.1 M KOH
CoP-PBSCF	This study	0.38 V	0.1 M KOH
H-PBSCF	This study	0.41 V	0.1 M KOH
CoP	This study	0.41 V	0.1 M KOH
A-PBSCF	This study	0.43 V	0.1 M KOH
$LaNiO_3$	J. Phys. Chem. Lett. 2013, 4, 1254	0.43V	0.1 M KOH
IrO_2/C	This study	0.45 V	0.1 M KOH
Mn_xO_y/N-C	Angew. Chem. Int. Ed., 2014, 53, 8508	0.46 V	0.1 M KOH
$MnCoFeO_4$	J. Mater. Chem. A 2014, 2, 16217	0.48V	0.1 M KOH
$LaCoO_3$	Nat. Commun. 2016, 7, 11510	0.49 V	0.1 M KOH
Layer by layer Co3O4/N-rGO	Adv. Mater. 2017, 30, 1703657	0.49 V	0.1 M KOH
$Ba_{0.5}Sr_{0.5}Co_{0.8}Fe_{0.2}O_{3-\delta}$	Angew. Chem. Int. Ed. 2015, 54, 3897	0.50 V	0.1 M KOH
$SrNb_{0.1}Co_{0.7}Fe_{0.2}O_{3-\delta}$	Angew. Chem. Int. Ed. 2015, 54, 3897	0.50 V	0.1 M KOH
$SrCo_{0.9}Ti_{0.1}O_{3-\delta}$	ACS Appl. Mater. Interfaces 2015, 7, 17663	0.51 V	0.1 M KOH

Table S3. Summary of the half-wave reduction potential for ORR ($E_{1/2}$) of catalysts in this work and other typical ORR catalysts in the literature.

Materials	Journal, Year, volume, first page	$E_{1/2}$ vs RHE	Electrolyte
Co_3O_4/N-rmGO	Nat. Mater., 2011, 10, 780	0.83 V	0.1 M KOH
Fe-TA-800	Angew. Chem. Int. Ed. 2016, 55, 12470	0.81 V	0.1 M KOH
CoP-PBSCF	This study	0.75 V	0.1 M KOH
N, S, O-doped mesoporous carbon	J. Am. Chem. Soc., 2014 136, 8875	0.75 V	0.1 M KOH
Nanostructured Mn oxide	J. Am. Chem. Soc., 2010, 132, 13612	0.75 V	0.1 M KOH
NBCaCF-1.5	Adv. Funct. Mater., 2016, 26, 4106	0.74 V	0.1 M KOH
H-PBSCF	This study	0.73 V	0.1 M KOH
$LaTi_{0.65}Fe_{0.35}O_{3-\delta}$ /N-doped C	Nano Energy, 2015, 15, 92	0.72 V	0.1 M KOH
A-PBSCF	This study	0.71 V	0.1 M KOH
$LaCu_{0.5}Mn_{0.5}O_3$	Nat. Chem. 2011, 3, 546	0.64 V	0.1 M KOH
Hollow spherical $La_{0.8}Sr_{0.2}MnO_3$	J. Power Sources, 2014, 271, 55	0.63 V	0.1 M KOH
CoP	This study	0.62 V	0.1 M KOH
Fe_3O_4/N-GAs	J. Am. Chem. Soc., 2012, 134, 9082	0.56 V	0.1 M KOH

Table S4. The potentials (vs RHE) for HER @ 10 mA cm^{-2} of the catalysts in this work and other non-noble-metal-based catalysts in the literature.

Materials	Journal, Year, volume, first page	Potentials	Electrolyte
np-(Co$_{0.52}$Fe$_{0.48}$)$_2$P	Energy Environ. Sci. 2016, 9, 2257	-79 mV	1 M KOH
CoP	This study	-209 mV	1 M KOH
MoB	Angew. Chen. Int. Ed. 2012, 51, 12703	-225 mV	1 M KOH
CoP-PBSCF	This study	-240 mV	1 M KOH
H-PBSCF	This study	-293 mV	1 M KOH
Ni/Ni(OH)$_2$	Angew. Chen. Int. Ed. 2012, 51, 12495	-300 mV	1 M KOH
NiFe LDH-NS@ defective graphene	Adv. Mater. 2017, 29, 1700017	-300 mV	1 M KOH
A-PBSCF	This study	-373 mV	1 M KOH
Co$_9$S$_8$@N, O, and S doped C	Adv. Funct. Mater. 2017, 27, 1606585	-320 mV	1 M KOH
Co-NRCNTs	Angew. Chem., Int. Ed. 2014, 53, 4372	-370 mV	1 M KOH

References

1	Kresse, G.; Hafner, J. Ab Initio Molecular Dynamics for Liquid Metals. *Phys. Rev. B* **1993**, *47*, 558–561.

2	Kresse, G.; Hafner, J. Ab Initio Molecular-Dynamics Simulation of the Liquid-Metal–amorphous-Semiconductor Transition in Germanium. *Phys. Rev. B* **1994**, *49*, 14251–14269.

3	Kresse, G.; Furthmüller, J. Efficiency of Ab-Initio Total Energy Calculations for Metals and Semiconductors Using a Plane-Wave Basis Set. *Comput. Mater. Sci.* **1996**, *6*, 15–50.

4	Kresse, G.; Furthmüller, J. Efficient Iterative Schemes for Ab Initio Total-Energy Calculations Using a Plane-Wave Basis Set. *Phys. Rev. B* **1996**, *54*, 11169–11186.

5	Blöchl, P. E. Projector Augmented-Wave Method. *Phys. Rev. B* **1994**, *50*, 17953–17979.

6	Kresse, G. From Ultrasoft Pseudopotentials to the Projector Augmented-Wave Method. *Phys. Rev. B* **1999**, *59*, 1758–1775.

7	Hammer, B.; Hansen, L. B.; Nørskov, J. K. Improved Adsorption Energetics within Density-Functional Theory Using Revised Perdew-Burke-Ernzerhof Functionals. *Phys. Rev. B* **1999**, *59*, 7413–7421.

8	Monkhorst, H. J.; Pack, J. D. Special Points for Brillouin-Zone Integrations. *Phys. Rev. B* **1976**, *13*, 5188–5192.

9	Choi, S.; Yoo, S.; Kim, J.; Park, S.; Jun, A.; Sengodan, S.; Kim, J.; Shin, J.; Jeong, H. Y.; Choi, Y.; et al. Highly Efficient and Robust Cathode Materials for Low-Temperature Solid Oxide Fuel Cells: $PrBa0.5Sr0.5Co2-xFe x O5+\delta$. *Sci. Rep.* **2013**, *3*, 2426.

10	Zhao, B.; Zhang, L.; Zhen, D.; Yoo, S.; Ding, Y.; Chen, D.; Chen, Y.; Zhang, Q.; Doyle, B.; Xiong, X.; et al. A Tailored Double Perovskite Nanofiber Catalyst Enables Ultrafast Oxygen Evolution. *Nat. Commun.* **2017**, *8*, 1–9.

11   Grimaud, A.; May, K. J.; Carlton, C. E.; Lee, Y.-L.; Risch, M.; Hong, W. T.; Zhou, J.; Shao-Horn, Y. Double Perovskites as a Family of Highly Active Catalysts for Oxygen Evolution in Alkaline Solution. *Nat. Commun.* **2013**, *4*, 1–7.

12   Hong, W.; Stoerzinger, K. A.; Lee, Y.-L.; Giordano, L.; Grimaud, A. J. L.; Johnson, A. M.; Hwang, J.; Crumlin, E.; Yang, W.; Shao-Horn, Y. Charge-Transfer-Energy-Dependent Oxygen Evolution Reaction Mechanisms for Perovskite Oxides. *Energy Environ. Sci.* **2017**, *10*, 2190–2200.

13   Jacobs, R.; Booske, J.; Morgan, D. Understanding and Controlling the Work Function of Perovskite Oxides Using Density Functional Theory. *Adv. Funct. Mater.* **2016**, *26*, 5471–5482.

14   Gong, Q.; Wang, Y.; Hu, Q.; Zhou, J.; Feng, R.; Duchesne, P. N.; Zhang, P.; Chen, F.; Han, N.; Li, Y.; et al. Ultrasmall and Phase-Pure W2C Nanoparticles for Efficient Electrocatalytic and Photoelectrochemical Hydrogen Evolution. *Nat. Commun.* **2016**, *7*.

15   Wu, H.; Xiao, W.; Guan, C.; Liu, X.; Zang, W.; Zhang, H.; Ding, J.; Feng, Y. P.; Pennycook, S. J.; Wang, J. Hollow Mo-Doped CoP Nanoarrays for Efficient Overall Water Splitting. *Nano Energy* **2018**, *48*, 73–80.

16   Nørskov, J. K.; Rossmeisl, J.; Logadottir, A.; Lindqvist, L.; Kitchin, J. R.; Bligaard, T.; Jónsson, H. Origin of the Overpotential for Oxygen Reduction at a Fuel-Cell Cathode. *J. Phys. Chem. B* **2004**, *108*, 17886–17892.

17   Liu, S.; Tao, H.; Zeng, L.; Liu, Q.; Xu, Z.; Liu, Q.; Luo, J.-L. Shape-Dependent Electrocatalytic Reduction of CO2 to CO on Triangular Silver Nanoplates. *J. Am. Chem. Soc.* **2017**, *139*, 2160–2163.

18   Zhang, R.; Tang, C.; Kong, R.; Du, G.; Asiri, A. M.; Chen, L.; Sun, X. Al-Doped CoP Nanoarray: A Durable Water-Splitting Electrocatalyst with Superhigh Activity. *Nanoscale* **2017**,

9, 4793–4800.

19   Cramer, C. J. *Essentials of Computational Chemistry Theories and Models*, Second Edi.;
John Willey & Sons Ltd: Chichester, 2004.

20   Rosen, J.; Hutchings, G. S.; Lu, Q.; Rivera, S.; Zhou, Y.; Vlachos, D. G.; Jiao, F.
Mechanistic Insights into the Electrochemical Reduction of CO2 to CO on Nanostructured Ag
Surfaces. *ACS Catal.* **2015**, *5*, 4293–4299.